Micro-kinetic modelling of photocatalytic CO2 reduction over undoped and N-doped TiO2

Andjelika Bjelajac, Drejc Kopač, Antoine Fecant, Eugénie Tavernier, Rada Petrović, Blaž Likozar, Djordje Janaćković

ARTICLE

Micro-kinetic modelling of photocatalytic CO_2 reduction over undoped and N-doped TiO_2

Received 00th January 20xx,
Accepted 00th January 20xx

DOI: 10.1039/x0xx00000x

Andjelika Bjelajac,*[a] † Drejc Kopač, [b] Antoine Fecant, [c] Eugenie Tavernier, [c] Rada Petrović, [d] Blaž Likozar [b] and Djordje Janaćković [d]

CO_2 photoreduction is studied using in-house synthetized undoped and N-doped TiO_2 nanoparticular photocatalysts. Comparison with the commercial P25 TiO_2 powder shows that the synthetized samples are more effective. P25 produced a negligible amount of CH_4, unlike the synthetized samples. N-doping of TiO_2 powder caused higher productivity rate of all product, and provided the best performance for CO_2 reduction. The average production rate of CH_4 was 0.191 µmol h^{-1} g^{-1}, whereas of CO was 0.111 µmol h^{-1} g^{-1}. The experimental data is used to fit the micro-kinetic modelling parameters. The kinetic constant of H_2O dissociation is the lowest for all tested samples, revealing that this is the rate-determining step. The kinetic constants for the H_2, CO, and CH_4 formation were of the same order for all catalysts samples, showing that the rates of these reactions are independent on the catalyst type.

[a.] *University of Belgrade, Innovation center of the Faculty of Technology and Metallurgy, Karnegijeva 4, 11000 Belgrade, Serbia*
[b.] *National Institute of Chemistry, Hajdrihova 19, SI-1001 Ljubljana, Slovenia*
[c.] *IFP Energies nouvelles, Rond-point de l'échangeur de Solaize, 69360 Solaize, France*
[d.] *University of Belgrade, Faculty of Technology and Metallurgy, Karnegijeva 4,11000 Belgrade, Serbia*
* Corresponding author: abjelajac@tmf.bg.ac.rs
† Present address: LPICM, Ecole Polytechnique, CNRS, IP Paris, 91128 Palaiseau, France
Electronic Supplementary Information (ESI) are available. See DOI: 10.1039/x0xx00000x

Introduction

The rise of CO_2 emission due to extensive fossil fuel combustion is a major environmental concern. Furthermore, the energy crisis arises since the fossil fuel sources are drying up. A way to deal with these issues is to reduce the concentration of CO_2 by converting it to less harmful, but also valuable products, such as CH_4 that can be directly used as a fuel, or CO that is also an important chemical feedstock and an essential component of syngas, a mixture of H_2 and CO. Syngas can be further converted to liquid hydrocarbon fuels through well-known Fischer-Tropsch synthesis. Much attention is given to studying the artificial photosynthesis phenomenon, which means reduction of CO_2 with H_2O in the presence of light and for that reaction a catalyst is required[1, 2]. When a photocatalyst absorbs photons whose energy is equal to or greater than the band gap of a catalyst, the charge carriers are generated. Electron from the valence band (VB) of a catalyst goes to the conductive band (CB) leaving behind a hole. The final step of the photocatalysis is the chemical reactions between surface species and charge carriers[3]. However, a high percentage of electron-hole pairs recombine. That depends on the rate of the separation and charge carrier transport. It was found that about 90% or more of the photogenerated electrons recombine within 10 ns[4]. Furthermore, not all the electrons reaching the surface can reduce CO_2 which is an inert and stable compound. The standard reduction potential of CO_2 to generate $\bullet CO_2^-$ is evaluated at E^o_{red} = -1.90 V vs the normal hydrogen electrode (NHE) (Table 1)[5, 6]. Even if most of publications on this topic propose $\bullet CO_2^-$ as an intermediate[7, 8], suggesting a mono-electronic activation of CO_2, this activation potential is very high and never reached by any semiconducting material. Other teams suggest that $\bullet CO_2^-$ may not be an intermediate for CO_2 photoreduction pathway thus implying an activation by a bi-electronic mechanism and allowing to reach lower potential to carry the reduction semi-reaction[9, 10]. Nevertheless, in order to reduce CO_2 into carbon monoxide or hydrocarbons, electrons in the CB of a semiconductor photocatalyst are required to have more negative chemical potential than the redox potentials of the corresponding reactions, while for water oxidation, holes in the VB need to lie on more positive potential level than water oxidation level[4]. This means the choice of semiconductor photocatalyst relays primary on its band gap levels positions. From a thermodynamic point of view, formation of methane and methanol are more favorable in CO_2 reduction than carbon monoxide, formaldehyde and formic acid, since these reactions take place at lower potentials (Table 1). However, the kinetic drawback makes methane and methanol formation more difficult because more electrons are required for the former reactions. Notwithstanding, the prospective debate concerning one- or bi-electronic activation pathway for CO_2, due to the complicated nature of the inorganic photocatalyst surface and no unreachable energetic barriers, the interaction between photocatalyst and absorbed species may undergo a series of one-electron/proton processes as long as the CO_2 activation has taken effect. Thus the actual redox potential required is determined by the reaction pathway.[11]

Table 1. Chemical reactions of CO_2 reduction and corresponding thermodynamic potential vs NHE

Chemical Equation	Thermodynamic potential, V
$CO_{2\,(g)} + e^- \rightarrow CO_2^-$	-1.90
$2H^+ + 2e^- \rightarrow H_{2(g)}$	0.00
$CO_{2(g)} + 2H^+ + 2e^- \rightarrow HCOOH_{(g)}$	-0.114
$CO_{2(g)} + 4H^+ + 4e^- \rightarrow HCHO_{(g)} + H_2O_{(g)}$	-0.072
$CO_{2(g)} + 2H^+ + 2e^- \rightarrow CO_{(g)} + H_2O_{(g)}$	-0.104
$CO_{2(g)} + 6H^+ + 6e^- \rightarrow CH_3OH_{(g)} + H_2O_{(g)}$	+0.031
$CO_{2(g)} + 8H^+ + 8e^- \rightarrow CH_{4(g)} + H_2O_{(g)}$	+0.169

Reduction of CO_2 by photogenerated electrons, should produce the equal number of photogenerated holes. If there is an excess of holes, the charge recombination will increase and the lifetime of electrons will be shortened. What is more, the holes can have negative impact on the photocatalytic reaction resulting in photocorrosion of the catalyst[12]. The way to deal this issue is to use an artificial electron donor to scavenge the holes, i.e. water that is considered as an ideal candidate, since it does not cause more CO_2 emission[11]. Furthermore, from both the thermodynamic and kinetic point of view, the reduction of water is more feasible than most of the CO_2 reduction reactions (Table 1). First, the reduction potential of water to hydrogen is more positive than the reduction potential of CO_2 reduction to CO, formic acid and formaldehyde and second, water reduction is just a 2-electrons process, unlike others which require 4–8 electrons or even more when C-C coupling. However, the concentrations of H_2O need to be optimized since the excessively high H_2O concentrations would occupy the catalyst active sites and consequently reduce the surface contact of CO_2 molecules with the photocatalyst[13].

Among many proposed semiconductors that are applied for CO_2 reduction, i.e. ZnO, CdS, TaNO, WO_3, GaP, SiC, ZrO_2, SnO_2, Ga_2O_3, $BiWO_3$, CdS, ZnS, GaN, SiC etc. TiO_2 is widely used due to its non-toxicity, wide abundance, low price, chemical/thermal stability and strong oxidative potential. However, the photocatalytic performances, such as rate production (number of mol of product in time vs mass of used catalyst) of TiO_2 are limited in particular by the fact that TiO_2 absorbs only UV part of the solar spectrum. Therefore, it was necessary to shift the absorption to visible range by i.e. doping with N. Our previous study showed that N-doped TiO_2 nanoparticles are able to degrade organic dye upon visible light illumination more efficiently than the undoped TiO_2. Since N-doped TiO_2 absorbed more photons, it provided more electrons and holes for degradation of dye. We assumed that doping would have the same effect also on CO_2 reduction[14]. In addition to this, only a few studies explored gas phase CO_2 photoreduction with water involving N-doped TiO_2[15, 16].

Moreover, N-doping induced formation of oxygen vacancies (V_O)[17] that serve as surface reactive sites (reacting with H_2O, for example)[18], and can also donate excess unpaired electrons to Ti atoms that are subsequently reduced into Ti^{3+}. These stored electrons may strongly affect the surface chemistry and charge transport properties of TiO_2[3]. V_O formed on the surface is considered to be electron-trapping centre that further inhibits the recombination process of the charges[19]. Di Valentin et al.[20] applied density functional theory calculations and showed that the formation energy of V_O in bulk anatase TiO_2 is drastically reduced in the presence of N-impurities, from 4.2 eV in pure TiO_2 to 0.6 eV in N-doped TiO_2. They explained it as a 'compensation' effect, meaning that the electrons in vacancy related states near the bottom of the conduction band can be transferred to empty nitrogen impurity states near the top of the valence band. This leads to a considerable energy gain.

The aim of this work was to explore the reaction pathway of CO_2 reduction using N-doped TiO_2 and to set up a model that can help us to understand the difference in productivity when compared to the undoped TiO_2, both synthetized and commercial P25. Our goal was to follow the thermodynamics and to explain the reaction pathway, leading ultimately to H_2, CH_4, and CO products. Micro-kinetic modelling helped us understand the kinetics of the reactions, and enabled us to compare the differences in the rate of reactions and the rate-determining steps among different photocatalysts.

The paper is organized as follows. We first present the experimental details, explaining the synthesis procedure and photocatalysts characterization. In results and discussion section, we present the experimental setup for CO_2 reduction and the experimental results, followed by the micro-kinetic model. The modelling results are discussed and compared with the experimental outcomes, giving clear perspective on reaction steps rates. We conclude in the last section.

Experimental

Samples preparation

The following reactants of p.a. grade were used for the synthesis of TiO_2: titanium tetrachloride ($TiCl_4$), titanium isopropoxide ($Ti(O_iPr)_4$) and cyclohexane (C_6H_{12}). The gels were synthetized in a glove box, under a protective atmosphere of nitrogen by the following procedure[21, 22]: 10 cm^3 $Ti(OC_3H_7)_4$ was mixed with 3.3 cm^3 of a solvent (cyclohexane), followed by adding of 3.7 cm^3 $TiCl_4$, drop by drop. The obtained mixture was heated in an autoclave at 160 °C for 3 h in order to form gel. The so-synthetized gel was dried at 100 °C under nitrogen flow. The undoped TiO_2 powder was obtained by gel annealing in air at 500 °C for 3 h. To follow the effect of thermal treatment on N doping and consequently the photocatalytic activity in CO_2 reduction the two conditions were set: the gel that was directly annealed in ammonia (NH_3) flow (200 cm^3/min) in a tube furnace, at 500 °C for 3 h, followed by natural cooling to room temperature under the NH_3 gas, was denoted as N-TiO_2(G), and the one that was pre-annealed in air at 500 °C for 3 h and then in NH_3 atmosphere at the same conditions was denoted as N-TiO_2(P). Both of the obtained samples were post-annealed in air at 400 °C for 30 min. For compassion with the synthetized samples, TiO_2 P25 Degussa from Aeroxide® was used.

Samples characterization

The high resolution transmission electron microscopy (HRTEM) was used for the estimation of the nanoparticles size. The micrographs were obtained using a Jeol JEM-2010 operating at 200 kV. The average size of the nanoparticles was determined by a manual measurement of about thirty nanoparticles per sample. The XRD analyses of the samples were done using a BRUKER D8 ADVANCE, with a Vario 1 focusing primary monochromator (Cu Kα1 radiation, λ = 1.54059 Å). The average crystallite size was calculated by using the Scherrer's equation like in the previous work[23]. The UV–Visible diffuse reflectance spectra (DRS) were recorded on a Shimadzu 2600 UV–Visible spectrometer with an integrating sphere attached and using $BaSO_4$ as a reference. The spectra were recorded in the wavelength range 300–600 nm. Using the Tauc plots of the transformed Kubelka–Munk function[23], the band gap

energy of the samples were determined. The Kubelka–Munk functions were calculated as F(R) = (1- R)/(2R), where R is reflectance in %. The absorbance data are also deduced from the DRS measurements.

Photocatalytic experiments

Photocatalytic experiments were carried out continuously in a stainless steel fixed bed reactor gas flow passing through the sample, operating at atmospheric pressure and ambient temperature. Typical sample masses involved are between 100 and 300 mg. CO_2:H_2O molar ratio (obtained by CO_2 bubbling in water tank) was fixed at 30:1 and CO_2 gas flow was fixed at 0.3 cc.min^{-1}, resulting in the total gas flow rate (CO_2 + H_2O) of 0.31 cc.min^{-1}. Irradiance for 315-600 nm wavelength range was adjusted to 380 W.m^{-2} and controlled with a radiometer equipped with CCD captor (Delta Ohm), corresponding to an overall Photon Flux Density (PFD) of 1.52.10^{-3} mol. s^{-1}.m^{-2}, and provided by a Xe lamp Max303 Asahi (equipped with a cut off filter for IR for wavelengths above 600 nm). Moreover, the reactor was fitted with an optical quartz window ($S_{irradiation}$ = 1.08.10^{-3} m^2) through which the light flux reaches the sample. Reagents and products were analysed online by a gas chromatograph TCD sensor micro-chromatograph Lan3000 (SRA Instruments, µGC-TCD). Gas phase analyses were performed every 10 minutes. The micro-chromatograph was calibrated for all gases from different gas cylinders with controlled contents purchased from Air Liquide. CO_2 was purchased from Air Liquide (purity > 99%). Water used for material synthesis and poured in the water tank for photocatalytic tests was demineralized water with a resistivity > 10 MΩ**.** A typical test duration is about 20 hours on stream.

Two parameters are calculated for each sample: average electron consumption rate – for measuring global activities as several products can be formed – (electron consumed vs time and mass of the photocatalyst), and the apparent effective quantum yield (the number of electrons that has been involved in product formation (i.e. 8 for CH_4 or 2 for H_2) divided by the number of absorbable photons regarding band gap values of the materials[24]). The average electron consumption rate for each catalyst, $\overline{r^{e^-}}$ in µmol.h^{-1}g^{-1}, and apparent effective quantum yield, $\Phi_{app.eff.}$, in %, were calculated using the following equation (1) and (2), respectively:

$$\overline{r^{e^-}} = \frac{1}{T.O.S.} \int_0^{T.O.S.} \sum_i \frac{n_i^{e^-} \times [i](t) \times Q_{tot}}{V_m^{25°C} \times m_{catalyst}} \times 60 \cdot dt \qquad (1)$$

$$\Phi_{app.eff.} = \frac{\overline{r^{e^-}} \times m_{catalyst} \cdot 10^{-4}}{PDF_{eff} \times S_{irradiation} \times 3600} \qquad (2)$$

Where $n_i^{e^-}$ is the stoichiometric coefficient of the electrons consumed by the product i (i.e. 2 e$^-$ are needed to form H_2 or CO, whereas CH_4 needs 8 electrons), [*i*](*t*) is the concentration of product i over time (in ppmVol), Q_{tot} is the CO_2 and H_2O input flow rate (3.1·10^{-4} L.min^{-1}), $V_m^{25°C}$ is the molar volume of a gas at 25°C (24.5 L.mol^{-1}), $m_{catalyst}$ is the mass of the catalyst (in g), and PFD_{eff} is the effective Photon Flux Density (in mol.s^{-1}.m^{-2}, taken from 315 nm to λ_{max} absorbable by the considered photocatalyst[24]). The PFD_{eff} was calculated on the basis on total lamp irradiance spectra (Fig. S1 in the supplementary file).

Prior to photocatalytic evaluation of materials, a test has been carried out with empty reactor without detection of any products aforementioned. Also, solids have been tested with argon replacing CO_2 gas, thus only water vapour is fed to the reactor, and no carbon containing products have been detected, only H_2 coming from water splitting. Average electron consumptions are given with a standard deviation of ± 10 % relative.

Experimental results served us to set a micro-kinetic model, applying a "top to bottom" approach. We started by making a wide reaction scheme of CO_2 reduction using TiO_2 catalyst. The reactions that led to formation of the products that were not obtained were not taken into account. Indeed, in our experiments we only observed gaseous products like H_2, CO, CH_4 and C2/C3 alkanes. Therefore, we assume the reaction pathway follows the scheme given in the supplementary file as Fig. S2. Similar CO_2 reduction mechanisms have been proposed in the literature and studied from the theoretical point of view on different catalysts[25,26]. These studies confirmed that material composition and architecture play a central role in the reaction pathway energetics.

Results and discussion

Photocatalysis

The photocatalytic results are summarized in Table 2, together with the properties of each sample. Concerning the synthetized samples, the information about the phase composition and crystallite size from XRD were taken from our previously published work[23], whereas the information about P25 were taken from the literature[27–30]. We also included the TEM measurements results, since we use those data for modelling calculations. The representative TEM micrographs are given in Fig. 1 a), whereas the particle size distribution of the three synthetized samples is provided in the supplementary file as Fig S3. The E_g values were deduced from the Tauc plots (Fig. 1 b)) using the DRS measurements. To demonstrate more clearly the absorbance red shift for the N doped samples, (iii) and (iv), compared to the undoped (ii) and the P25 TiO_2 (i),

the absorption spectra are also provided in Fig. 1 c). The narrowing of the band gap and the absorbance red shift for the N doped samples is a result of the interstitial incorporation of nitrogen in TiO_2 structure, as it was concluded according to XPS analysis of the samples[23]. The new inter band level is characteristic for interstitially incorporated N as it is the case here. The nitrogen incorporation was more efficient by the gel annealing in ammonia (N-TiO_2(G)) than by the annealing of the sample that was pre-annealed in air (N-TiO_2(P)). Therefore, narrowing of the band gap and absorbance red shift were higher for N-TiO_2(G) than for N-TiO_2(P).

Table 2 Properties of the investigated samples and the photocatalytic results.

Sample	Phase composition	Crystallite size from XRD, nm	Particle size from TEM, nm	E_g, eV	Apparent effective quantum yield, %	Average electron consumption rate, $\mu mol.h^{-1}.g^{-1}$
P25 TiO_2	~ 80 % anatase, ~20 % rutile	25 (average primary particle size)	37.0[a]	3.15	0.011	0.363
Undoped TiO_2	anatase	14.1	8.3 ± 1.6	3.13	0.042	0.568
N-TiO_2(G)	anatase	8.2	6.9 ± 0.9	2.67	0.035	1.722
N- TiO_2(P)	anatase	15.3	11.0 ± 1.8	2.74	0.051	2.471

[a] *as P25 TiO_2 is a mixture of crystalline phases, XRD size determination could lead to much lower crystalline size than TEM measurements that provide the value for particles composed of several crystalline domains*.

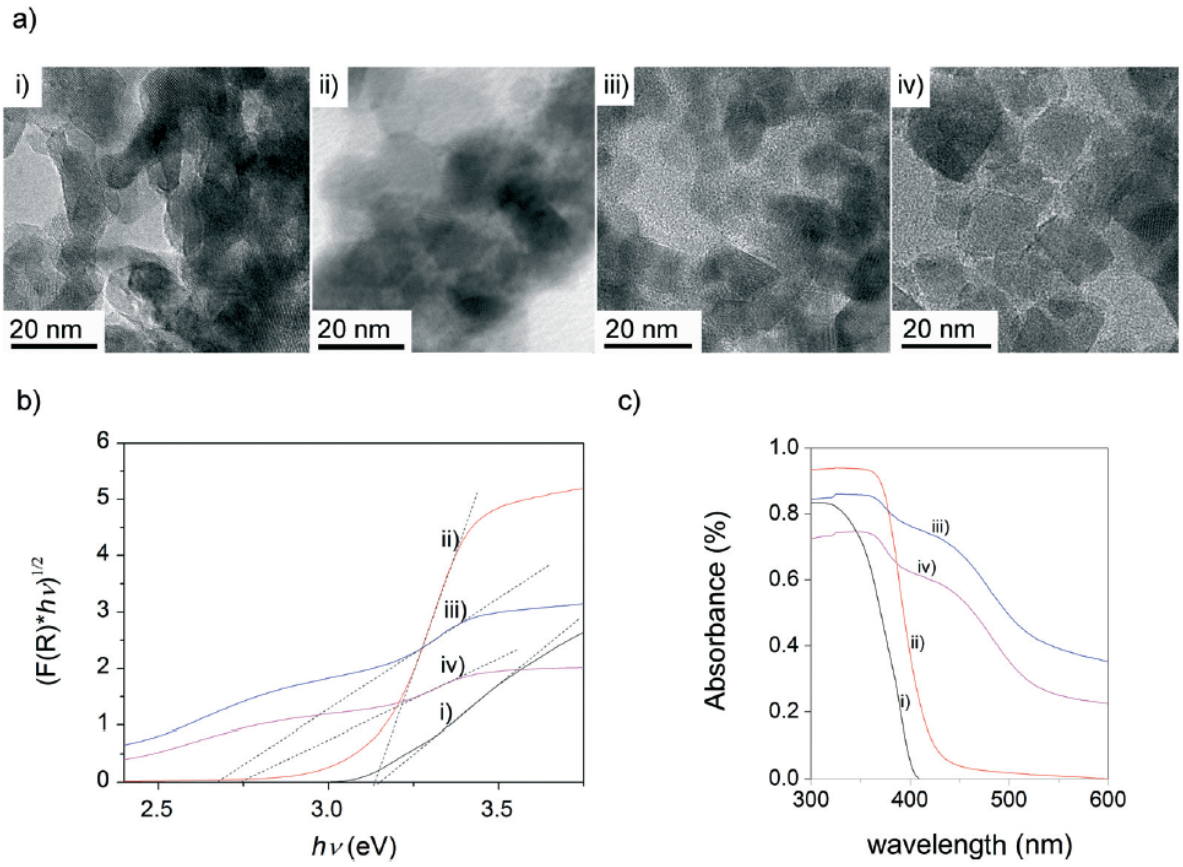

Fig. 1 a) TEM micrographs, b) Tauc plots and c) adsorption spectra of the investigated samples: i) P25 TiO_2, ii) undoped TiO_2, iii) N-TiO_2(G) and iv) N-TiO_2(P).

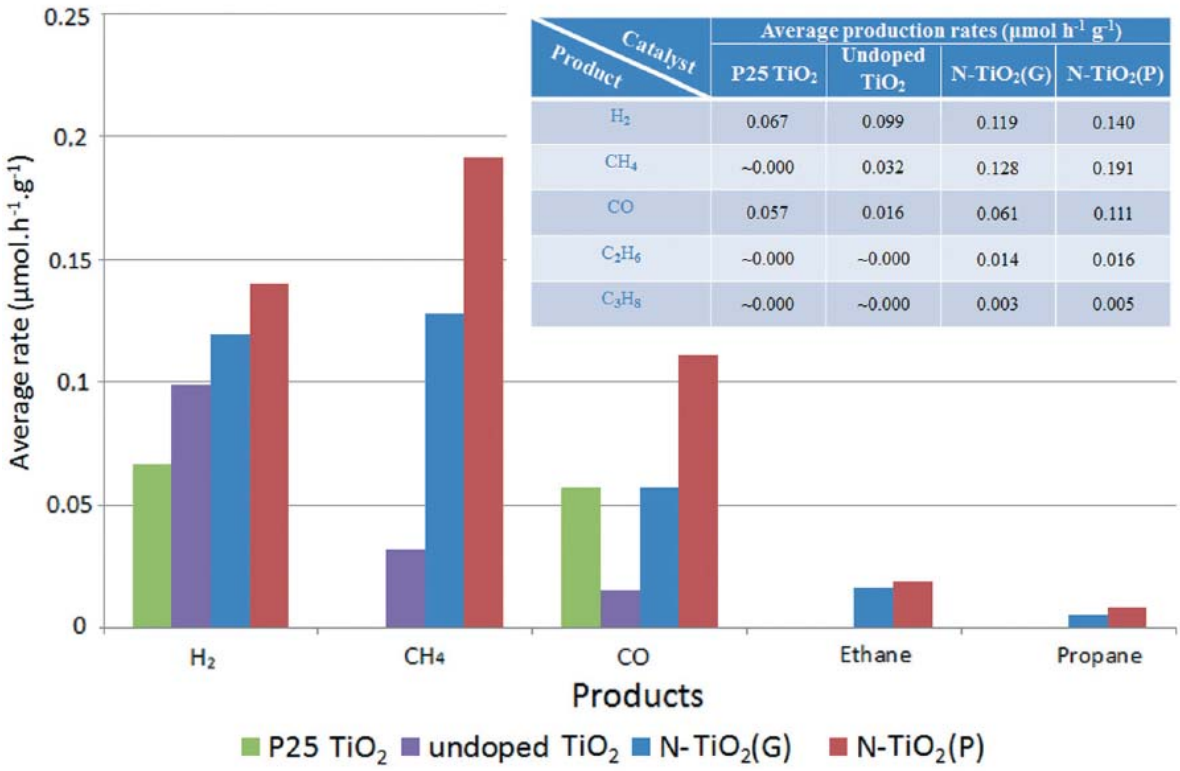

Product \ Catalyst	Average production rates (µmol h^{-1} g^{-1})			
	P25 TiO_2	Undoped TiO_2	N-TiO_2(G)	N-TiO_2(P)
H_2	0.067	0.099	0.119	0.140
CH_4	~0.000	0.032	0.128	0.191
CO	0.057	0.016	0.061	0.111
C_2H_6	~0.000	~0.000	0.014	0.016
C_3H_8	~0.000	~0.000	0.003	0.005

Fig. 2 Average production rates of each product for all catalysts.

The apparent effective quantum yield values go in the following order: N-TiO_2(P) > undoped TiO_2 > N-TiO_2(G) > P25. We assume that the smallest apparent effective quantum yield for P25 is partly due to the phase composition. It is likely that the synthetized samples consisting of pure anatase phase is preferable for efficient photocatalytic reactions, compared to the mixed phase P25 powder. However, a mixture of anatase and rutile phases has been reported to be more active than either of the pure phases alone[31]. The high activity of the mixture of phases has been attributed to the separation of photoexcited charge carriers between the two phases. In this mixed-phase of TiO_2, anatase is considered to be an active component, while rutile is conventionally considered to act as an electron sink because of the lower conduction band energy than that of anatase. However, there is still a controversy over the alignment of the conduction band minima of rutile and anatase phases but the experimental results suggest that the photoexcited electrons of rutile TiO_2 are less active than those of anatase[32]. Furthermore, by comparing the apparent effective quantum yield values for the synthetized samples, we can see that they are in accordance with the corresponding crystallite size, meaning that with smaller crystallites the recombination is higher, therefore smaller number of electrons are used for CO_2 reduction. Koci et al. reported that there is an optimal crystallite size of TiO_2 anatase photocatalyst for photoreduction of CO_2. They showed that with increasing the crystallites size to 14 nm, the photoreduction of CO_2 is enhanced, but the production yield is smaller for the TiO_2 catalyst of the 29 nm sized crystallites[33]. Also in another work they showed that the photoreactivity of TiO_2 increases as the particle size is decreased from 26 nm to 18 nm[34]. This is in accordance with our results, since the average primary particle size of the P25 sample is 25 nm[27, 28], whereas the crystallites of the synthetized samples are 15 nm and smaller.

As the average electron consumption rate is the direct measurement of light utilization efficiency, the reported results should be in accordance with the band gap values. However, the highest average electron consumption rate was achieved for N-doped TiO_2(P) (Table 2), but N-doped TiO_2(G) has a narrower band gap, meaning more electrons should be produced in the case of N-doped TiO_2(G). Nevertheless, as already mentioned, the crystallite size affects the recombination, thus in the case of N-doped TiO_2(P) the crystallite size is the optimal, and the recombination is the smallest leading to the highest average electron consumption rate.

Additional comparison of the catalysts performances was done by measuring the average production rate for each product (Fig. 2). The equation (1) was used for these calculations. For each product i, the production rate, $\overline{r^i}$, was calculated by removing stoichiometric coefficient from the equation and considering only product i concentration and not the sum of all, like for the global electron consumption. A table with the production rates is in the insert of the figure. By analyzing the results one can see that the main difference was that in the case of P25 there was no CH_4 detected, only CO and H_2. This was also observed by Zhao et al.[35] where the main product of CO_2 reduction with H_2O using P25 was CO. We assume that donation of electrons coming from water splitting is not efficient enough to produce excess of H for CH_4 formation. From the kinetic point of view, the formation of CO is favored since it requires only 2 electrons compared to the formation of CH_4 which needs 8 electrons (Table 1)[4, 35]. Given that the undoped TiO_2 has higher average electron consumption rate than P25 (Table 2), more electrons are photogenerated and used for the production of H_2, CO and CH_4. For the undoped TiO_2, the highest productivity rate was for H_2, then CH_4 and CO. On the other hand, for the N doped samples, among all detected products (H_2, CH_4, CO, C_2H_6 and C_3H_8), the CH_4 production rate was the largest.

We note that higher number of excited electrons, due to smaller band gaps of N doped samples, provide more H_2 and more CH_4 than in the case of the undoped TiO_2. As seen from Fig. 2, for both N doped samples, the amount of H_2 produced is not higher than of CH_4, which means that water splitting reaction is not dominant, like it was reported by Phongamwong et al. where the rate production of H_2 was two order of magnitude higher than of CH_4[18]. Furthermore, when comparing the two N doped samples with each other, the N-TiO_2(P) provided higher amount of all detected products, even though it has a narrower bang gap than N-TiO_2(G) and the amount of incorporated N is smaller[23]. The primary reason can be again the bigger crystallites of N-TiO_2(P) than of N-TiO_2(G) meaning less recombination of photogenerated electron-hole pairs happens and more efficient the light utilization is, which is in accordance with the results of average electron consumption rate (Table 1). On the other hand, semiconducting photocatalysts have been recently engineered to improved CO_2 conversion by creating intrinsic defects like oxygen vacancies, Vo[36]. It was shown that both the surface oxygen vacancies and bulk single electron trapped oxygen vacancies (SETOVs), formed by i.e. doping by nitrogen, contributed to the enhancement of the light absorption. However, while the surface vacancies facilitated the separation of the photogenerated charge carriers, the bulk SETOVs acted as the recombination center[37]. The photoreduction efficiency of CO_2 was improved with the increase of the ratio of surface oxygen vacancies to bulk SETOVs, but the concentration of both vacancies needed to be optimized: i) the bulk SETOVs, to provide visible-light absorption and minimize recombination, and ii) the surface Vo, to prevent the formation of defect-related recombination centers in the case of excessive Vo. In our case, we assume the N-TiO_2(P) has lower concentration of both bulk Vo, due to lower N content, and surface Vo, due to bigger crystallites in comparison to N-TiO_2(G), but the surface/bulk Vo ratio is obviously higher than for N-TiO_2(G) and the productivity rate for all compounds is higher, especially for CH_4.

The selectivity of the used catalysts, which is relatively poor, can be increase by optimization of processing parameters or by further modification of the catalysts. For example, the selectivity of CH_4 production can be increased if both H_2 and H_2O are used as reductants and/or if low initial CO_2 concentrations is applied[38]. Although CH_4 formation is thermodynamically more feasible than CO (Table 1), it requires more electrons and protons and thus is kinetically limited. The deposition of noble metal nanoparticles, for example Pt, can enrich the electron density that enhances the probability of multi-electron reaction, such is formation of CH_4. In addition, strong adsorption of CO as an intermediate for CH_4 production on highly electron donating noble metal sites favours total reduction to CH_4[39]. What is more, noble metal nanoparticles are beneficial for the dissociation of H_2O and production of the activated H species, that are necessary for CH_4 production[36]. However, the importance of choosing an adequate noble metal, tailoring the size of nanoparticles in appropriate range and avoiding the oxidation of noble metal to metal oxide, was indicated[40].

Micro-kinetic modelling

We followed a “top to bottom” approach for the micro-kinetic modelling, meaning that the experimental data (Fig. 3) were used to fit the kinetic model of the photocatalytic reduction of CO_2 for four catalysts. Only the production of CH_4, CO and H_2 were considered in the model, since the amounts of C_2H_6 and C_3H_8 when produced were assumed as negligible.

The reaction pathway follows the equations 3-12. The formation of reactive electron and hole at the surface by photon absorption is assumed non-limiting step, so it was not modelled. Also, it is considered that electrons and holes do not occupy a surface site, meaning that an active site carrying an electron or a hole still may adsorb chemical species. Thus, our reaction pathway consists of

4 surface reactions and 6 gaseous adsorption/desorption reaction steps, as shown in Eqs. 3-12[41]:

$$CO_2(g) + 1^* \xleftrightarrow{k^{CO_2}} CO_2{}^* \quad (3)$$

$$H_2O(g) + 1^* \xleftrightarrow{k^{H_2O}} H_2O^* \quad (4)$$

$$2H_2O^* + 3^* \xrightarrow{k_1} 4H^* + O_2{}^* \quad (5)$$

$$2H^* \xrightarrow{k_2} H_2{}^* + 1^* \quad (6)$$

$$CO_2{}^* + 2H^* \xrightarrow{k_3} CO^* + H_2O^* + 1^* \quad (7)$$

$$CO_2{}^* + 8H^* \xrightarrow{k_4} CH_4{}^* + 2H_2O^* + 6^* \quad (8)$$

$$CO(g) + 1^* \xleftrightarrow{k^{CO}} CO^* \quad (9)$$

$$O_2(g) + 1^* \xleftrightarrow{k^{O_2}} O_2{}^* \quad (10)$$

$$H_2(g) + 1^* \xleftrightarrow{k^{H_2}} H_2{}^* \quad (11)$$

$$CH_4(g) + 1^* \xleftrightarrow{k^{CH_4}} CH_4{}^* \quad (12)$$

where * indicates the empty active surface site[42]. Firstly, all reactions were assumed reversible, but due to strong parameter correlations and large span of possible parameter values, we later assumed all surface reactions (apart from adsorption/desorption reactions) to be forward direction only, as indicated by arrows.

The micro-kinetic model assumes all reactions are first order[38]. For gaseous reactions (Eqs. 3, 4, 9-12), the adsorption contribution for gaseous species to the rate equation is modelled as

$$r_{ads}^{G} = k_{fwd}^{G}\theta_{empty} G R_{gas} T \quad (13)$$

where k^{G}_{fwd} is the fitting parameter for the forward rate coefficient of gaseous species (Eqs. 3, 4, 9-12), ϑ_{empty} is the surface coverage of empty sites, G is the gas fraction, R_{gas} is the gas constant and T is the temperature. The desorption contribution to rate for gaseous species is simply

$$r_{des}^{G} = k_{rev}^{G}\theta_{gas} \quad (14)$$

where k^{G}_{rev} is the fitting parameter for the reverse rate coefficient of gaseous species, and ϑ_{gas} is the gas surface coverage. Altogether, the 6 differential equations to describe temporal evolution of gaseous species are given in the form of (for each G = CO_2, H_2O, O_2, H_2, CO, and CH_4):

$$\frac{\partial G}{\partial t} = (-r_{ads}^{G} + r_{des}^{G}) f + (G_{in} - G) \times \frac{V_g}{V_r} \quad (15)$$

where f represents the factor of available surface sites for gas interaction, G_{in} is the gas inflow (in our case, only CO_2, H_2O and small amount of O_2 gases were inflow gases), V_g = 0.0003066 l min^{-1} is the gas volumetric flow throughout the reactor, and V_r = 0.01542 l is the reactor volume. The factor f is defined as:

$$f = \frac{N}{V_{cat}\varepsilon} \quad (16)$$

where N is the number of active surface sites in mol (different among different catalyst samples), V_{cat} = 0.0005 l is the volume of the catalyst, and ε is the void fraction within the catalytic bed, which we assumed ε = 0.9241 (calculated by the mass and volume of the sample compared to the bulk density of the catalyst). For surface reactions, the differential equations to describe temporal evolution of surface coverage with each intermediate are modelled as:

$$\frac{\partial \theta_{CO_2}}{\partial t} = r_{ads}^{CO_2} - r_{des}^{CO_2} - k_3\theta_{CO_2}\theta_H - k_4\theta_{CO_2}\theta_H \quad (17)$$

$$\frac{\partial \theta_{H_2O}}{\partial t} = r_{ads}^{H_2O} - r_{des}^{H_2O} - 2k_1\theta_{H_2O}\theta_{empty} + k_3\theta_{CO_2}\theta_H + k_4\theta_{CO_2}\theta_H \quad (18)$$

$$\frac{\partial \theta_{O_2}}{\partial t} = r_{ads}^{O_2} - r_{des}^{O_2} + k_1\theta_{H_2O}\theta_{empty} \quad (19)$$

$$\frac{\partial \theta_{H_2}}{\partial t} = r_{ads}^{H_2} - r_{des}^{H_2} + k_2\theta_H \quad (20)$$

$$\frac{\partial \theta_{CO}}{\partial t} = r_{ads}^{CO} - r_{des}^{CO} + k_3\theta_{CO_2}\theta_H \quad (21)$$

$$\frac{\partial \theta_{CH_4}}{\partial t} = r_{ads}^{CH_4} - r_{des}^{CH_4} + k_4\theta_{CO_2}\theta_H \quad (22)$$

$$\frac{\partial \theta_H}{\partial t} = 4k_1\theta_{H_2O}\theta_{empty} - 2k_2\theta_H - 2k_3\theta_{CO_2}\theta_H - 8k_4\theta_{CO_2}\theta_H \quad (23)$$

$$\frac{\partial \theta_{empty}}{\partial t} = \sum_G (-r_{ads}^{G} + r_{des}^{G}) - 3k_1\theta_{H_2O}\theta_{empty} + k_2\theta_H + k_3\theta_{CO_2}\theta_H + 6k_4\theta_{CO_2}\theta_H \quad (24)$$

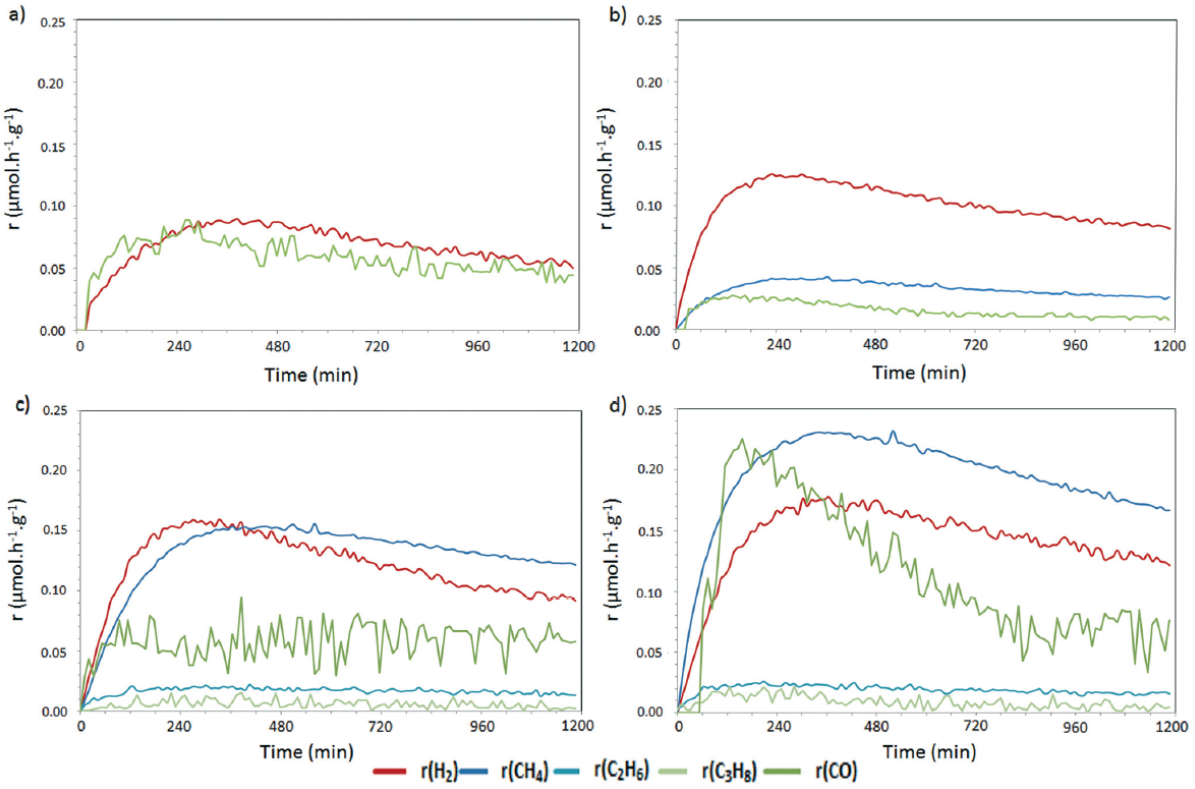

Fig. 3 Rate production over 20 hours on stream using: a) P25 TiO_2, b) undoped TiO_2, c) N-TiO_2(G) and d) N-TiO_2(P) catalysts.

where only the forward direction of reactions were considered to simplify the scheme, otherwise the terms for reverse reactions should also be added to the above equations. Also, all reactions were assumed as the first order reactions, so all ϑ enter the terms only once. Stoichiometry is taken into account.

Solving the model. Overall, the system of 14 ordinary differential equations was solved using Scipy odeint package (Python), which is based on lsoda from the FORTRAN library odepack. The system is fitted with Levenberg-Marquardt algorithm using lmfit package (Python). Initially, 17 free parameters were considered in the system, but this was later reduced to only 4 free parameters when fixing certain parameters, as follows. First, for gaseous species adsorption and desorption, the non-activated adsorption ($E_A \approx 0$) was assumed, meaning that the rate for the elementary reaction based on the Arrhenius equation is only the pre-exponential factor. Considering this, it was further assumed that the pre-exponential factor for gas adsorption can be approximated with:

$$k^{G}_{fwd} = \frac{P \times A}{\sqrt{2\pi m^{G} k_B T}} \quad (25)$$

where P is the gas pressure (assuming 1 bar), A is the effective area of the reaction site (calculated to be of the order of A ≈ 0.1 nm^2 for TiO_2), and m^G is the mass of the gas molecule[43]. It should be noted that the contribution of partition functions (vibrational, rotational and translational) was neglected. Similarly, for the gas desorption, the pre-exponential factor and thus the rate can be approximated with:

$$k^{G}_{rev} = \frac{k_B T}{h} \quad (26)$$

where h is the Planck's constant. At room temperature (300 K), the above equations give the estimates of k^G_{fwd} of the order of 10^8 s^{-1} to 10^9 s^{-1} (depending on the gas), while $k^G_{rev} \approx 6 \cdot 10^{12}$ s^{-1}. To simplify the fitting procedure, the rates for adsorption and desorption were fixed. In principle they could have been left as free parameters of the fit, accounting also for the contribution of the partition functions, but the testing showed that the overall results do not change significantly if they were left fixed. Thus, the k^G_{fwd} and k^G_{rev} in Eqs. 13 and 14 were fixed to the estimated values.

To solve Eqs. 15 and 17-24, the initial values have to be assumed. The system was tested by decoupling the reactions to obtain the initial rate assessment. All G_0 and ϑ_0 were assumed to be 0 except G_0^{CO2} and G_0^{H2O} for which the initial fractions were known (97% for CO_2 and 3% for H_2O). For the initial value of empty sites ($\vartheta_{empty,0}$),

we used the experimentally determined value for each catalyst, calculated using the following expression:

$$\theta_{empty,0}(mol) = \frac{m_{TiO_2}}{M_{TiO_2}} D_{TiO_2} \quad (27)$$

where D_{TiO2} corresponds to TiO_2 dispersion considering the spherical model and expressed by:

$$D_{TiO_2} = \frac{n_{TiO_2}^{surface}}{n_{TiO_2}^{particle}} = \frac{\frac{Surface_{particle}}{Section_{TiO_2}}}{\frac{Volume_{particle}}{Volume_{TiO_2}}} = \frac{6V_{TiO_2}}{Section_{TiO_2} d_{particle}} \quad (28)$$

The values for the nanoparticles size, $d_{particle}$, were taken from Table 2 using TEM measurements. The V_{TiO2}, which is the volume of a TiO_2 cluster, was calculated to be 0.034205 nm^3 and the $Section_{TiO2}$, which is the section of a TiO_2 cluster, was calculated to be 0.127394 nm^2 and they were the same for all the catalysts. These calculations were made by using crystallographic data for anatase TiO_2 given in Material Studio 7.0 software by Accelerys ®.

Thus, the initial values of empty sites ($\vartheta_{empty,0}$) were 4.50 x 10^{-4} mol for N-TiO_2(P), 6.45 x 10^{-4} mol for N-TiO_2(G), 8.86 x 10^{-4} mol for undoped TiO_2, and 9.27 x 10^{-4} mol for the reference P25, and they were left fixed during the fitting procedure.

All other values of the fit, which include k_1-k_4 surface reaction rates, were left as free parameters. We used the initial value of 10^{13} s^{-1} for the surface reaction rates[42].

Modelling results and discussion. The output of the catalytic CO_2 conversion to CH_4 from 4 different catalysts: N-TiO_2(G), N-TiO_2(P), undoped TiO_2 and the reference P25 catalyst was fitted. Table 3 shows the results of the fit, where k_1 is the kinetic constant for water splitting, whereas k_2, k_3 and k_4 are for H_2, CO and CH_4 production, respectively (equations (5-8)). Fig. 4 presents the fitted results together with the experimental data points. Note that k_3 and k_4 parameters are many orders of magnitude larger than other parameters, and thus do not vary much with respect to other parameters. Also, when assessing the initial rate, we noticed that if the reaction is fast, i.e., the activation energy is close to 0, then the surface reaction rate can be approximated by k_BT/h, which is again of the order of 10^{13} s^{-1} at room temperature. It can be noticed that for the P25 sample, the k_4 was left fixed at 0, since CH_4 production was negligible.

Table 3 Results for reaction rate coefficients for all four catalysts, as obtained from micro-kinetic modelling. The rates are given in s^{-1}.

Parameter	TiO_2 P25	Undoped TiO_2	N-TiO_2(G)	N-TiO_2(P)
k_1	3.8 ± 3 x 10^{-2}	20.0 ± 0.2	10.0 ± 0.3	80 ± 1
k_2	3 x 10^8 ± 3 x 10^4	10 x 10^8 ± 3 x 10^4	8 x 10^8 ± 3 x 10^5	3 x 10^8 ± 2 x 10^4
k_3	4 x 10^{12} ± 7 x 10^4	3 x 10^{12} ± 1 x 10^5	4 x 10^{12} ± 1 x 10^6	5 x 10^{12} ± 2 x 10^6
k_4	0	8 x 10^{12} ± 6 x 10^5	9 x 10^{12} ± 5 x 10^6	10 x 10^{12} ± 1 x 10^6

The obtained k rates cannot be used directly to extract the activation energy, since pre-exponential factors were approximated. In principle, this could be done via inverse Arrhenius law, but since we do not know precisely the pre-exponential factor (neglecting the contribution of partition functions), and even more importantly, since treating all surface reactions as first order, the rates can be absolutely over- or under-determined by many orders of magnitude. Nevertheless, the relative comparison is still valid, since all four samples were fitted with the same model.

We note that the trend of measurement does not necessary follow the fitted curve over total time span of the experiment (70,000 seconds). This is particularly visible on the CO yield for N-TiO_2(P) or H_2 yield for N-TiO_2(G). This can be due to the fact that on such a long time-scale, the catalyst can have episodes of activation and deactivation, the latter especially if the number of active sites change during the course of reactions due to catalyst surface becoming poisoned with intermediates. This was not taken into account in our model, so all the fitted curves are steady after the initial rise.

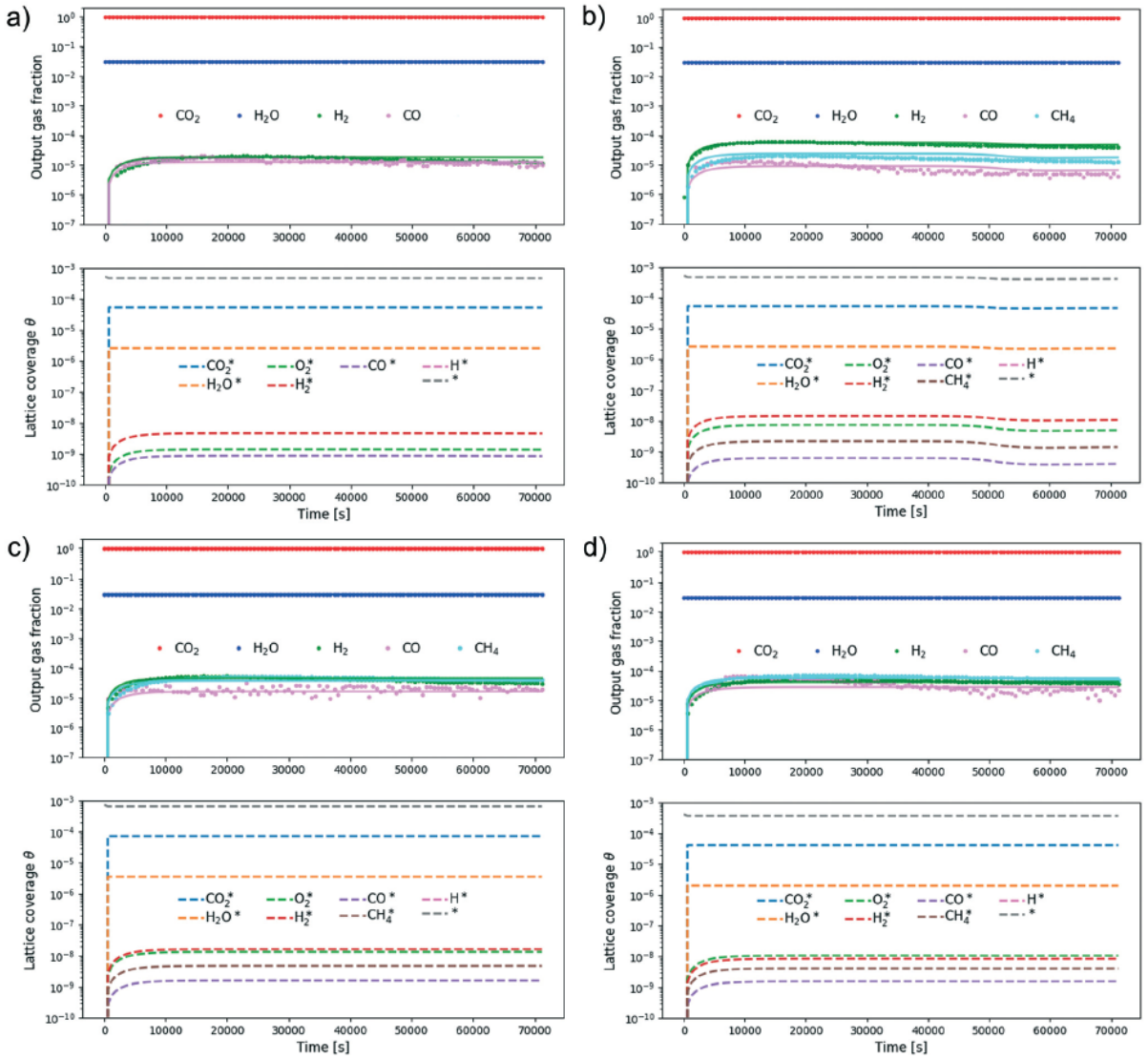

Fig. 4 Output gas fraction (top) and the lattice coverage (bottom) over time for: a) P25 TiO_2, b) undoped TiO_2, c) N-TiO_2(G) and d) N-TiO_2(P) samples. In output gas fraction plots, the solid lines represent the model, while the points are the measurements as obtained from Fig 3.

Comparing the obtained reaction rates, we notice that for N-TiO_2(P) catalyst, the rate k_1 for H_2O dissociation to H* and O_2 is the highest, but it is the lowest for P25. The kinetic constants for the second reaction k_2 are similar and of high value for all the catalysts meaning that formation of H_2 from H* does not depend on the catalyst. The k_3 and k_4 rates that account for the formation of CO and CH_4, respectively, are the highest for N-TiO_2(P), which is reflected also in experiments, since this catalyst produces the most CH_4 and also CO. We also note that both k_3 and k_4 rates are much higher than k_1 and k_2, meaning that those reaction steps are the quickest (fast reactions). The rate-determining step as obtained from the model is thus the water dissociation (k_1), which is the slowest reaction, confirming the experimental results.

The k_1 values follow the same order as the apparent effective quantum yield from the experiment (Table 3): N-TiO_2(P) > undoped TiO_2 > N-TiO_2(G) > P25. Since the apparent effective quantum yield shows the effectiveness of the absorbable photons to produce electrons for the product formation, it is not surprising the trend is the same. The water dissociation depends greatly of the amount of absorbable photons but also is effected by the materials composition, i.e. the recombination of the electron-hole pairs is higher in the case of smaller crystallites. Since for water dissociation to oxygen and H radicals a hole is needed, higher the recombination is, slower the water dissociation is[33]. However, in the case of P25, the crystallites size (25 nm) is above the optimal (14 nm) and it leads to smaller photoreactivity. We also commented that pure anatase

is beneficial for this photocatalytic application, unlike the mixed phase of the P25 catalyst.

To our knowledge, this work constitutes the first attempt for micro-kinetic approach of the photocatalytic reduction of CO_2 with H_2O. In the previous studies about kinetics of CO_2 reduction using TiO_2 nanoparticles the Langmuir–Hinshelwood model was used for rate determination of the adsorption of the reactants and desorption of products over the catalyst surface. Also the difference to our work was that the CO_2 reduction was with CH_4 and N_2 in the feed[44]. Another study, where the Langmuir–Hinshelwood model was used for the adsorption–desorption rates, illustrated the effect of indium loading on TiO_2 photocatalytic activity for transformation of CO_2 with H_2O to CO and CH_4 [45]. However, there is no study about micro-kinetics providing the insight of rate determination step.

Conclusions

In this study, TiO_2 nanoparticular photocatalysts were synthetized using a non-hydrolytic sol-gel method, where the gel and undoped powder were annealed in NH_3 atmosphere to induce the doping with N. The photocatalytic activity of the samples was tested for CO_2 reduction and they were compared to the results of TiO_2 P25 commercial powder. This study showed that the synthetized samples were more effective compared to the TiO_2 P25, most probably due to smaller band gaps and consequently higher photon absorption of the synthetized samples than of P25. The additional reason may be the optimal crystallite sizes of the synthetized samples and also due to phase composition of pure anatase, unlike the mixed anatase-rutile phase of P25. The most important difference comparing to P25 was that P25 catalyst did not produce CH_4 like the synthetized samples. The N-doping caused higher productivity rate of H_2, CH_4 and CO compared to the undoped TiO_2. Doping of the TiO_2 powder provided better performances of the catalyst compared to the N-doped TiO_2 obtained by annealing of gel in NH_3, even though the catalyst obtained by N doping of TiO_2 powder has higher band gap, meaning it absorbed less photons and thus might produce less active electrons and holes. However, the larger crystallite size provided lower recombination of charge carriers and thus higher electron consumption rate.

The experimental data were used to fit the micro-kinetic modelling parameters. The obtained model provided the insight into the reaction pathway and kinetics. We established that the water dissociation to H radical and O_2 is the slowest reaction, meaning it is the rate-determining step. The kinetic constant for H_2O dissociation is the highest for N-doped TiO_2 from powder and the lowest for P25. The kinetic constants for the formation of H_2 from H radicals are of high value and similar for all the catalysts meaning that H_2 formation does not depend of the catalyst. The rates that account for the formation of CO and CH_4 from adsorbed CO_2 and H radicals are even higher meaning that those reaction steps are the quickest. To our knowledge, this work constitutes the first attempt for micro-kinetic approach of the photocatalytic reduction of CO_2 with H_2O in the gas phase. The model developed here could be useful to deduce the rate and product yield at any particular reaction time and could aid as a tool for future optimization study.

ARTICLE

Conflicts of interest

There are no conflicts to declare.

Acknowledgements

The Serbian authors acknowledge with thanks the financial support of the Ministry of Education, Science and Technological Development, Republic of Serbia through the Projects III 45019. A. B. is grateful to EIT Climate KIC to participate in the program "Pioneers into Practice 2018". D. K. and B. L. acknowledge the funding from the Slovenian Research Agency (ARRS) through Core Grant P2-0152 and Project J2-7319.

Notes and references

1 S. Xie, Q. Zhang, G. Liu, Y. Wang, *Chem. Commun.,* 2016, **52**, 35–59.
2 J. Wu, Y. Huang, W. Ye, Y. Li, *Adv. Sci.,* 2017, **4**, 1–29.
3 S. R. Lingampalli, Mohd Monis Ayyub, C. N. R. Rao, *ACS Omega,* 2017, **2**, 2740–2748.
4 H. Abdullah, M. M. R. Khan, H. R. Ong, Z. Yaakob, *J. CO_2 Util.*, 2017, **22**, 15–32.
5 R. Parsons et J. Jordan (ed.) A. J. Bard, Standard potentials in aqueous solutions, Marcel Dekker, New-York, 1985.
6 S. G. Bratsch, *J. Phys. Chem. Ref. Data.,* 1989, **18,** 1–21.
7 E. Karamian, S. Sharifnia, *J. CO_2 Util.*, 2016, **16,** 194–203.
8 S. N. Habisreutinger, L. Schmidt-Mende, J. K. Stolarczyk, *Angew. Chemie - Int. Ed,.* 2013, **52,** 7372–7408.
9 S. Bernadet, E. Tavernier, D. Ta, R. A. L. Vallée, S. Ravaine, A. Fécant, R. Backov, *Adv. Funct. Mater.,* 2019, **29**, 1807767–1807774.
10 T. Inoue, A. Fujishima, S. Konishi, K. Honda, *Nature,* 1979, **277**, 637–638.
11 M. Tahir, N.S. Amin, *Energy Convers. Manag.*, 2013, **76**, 194–214.
12 K. Li, X. An, K. H. Park, M. Khraisheh, J. Tang, *Catal. Today,* 2014, **224**, 3–12.
13 A. Sarkar, E. Gracia-Espino, T. Wågberg, A. Shchukarev, M. Mohl, A. R. Rautio, O. Pitkänen, T. Sharifi, K. Kordas, J. P. Mikkola, *Nano Res.,* 2016, **9**, 1956–1968.
14 M. Tahir, B. Tahir, Appl. Surf. Sci., 2016, **377**, 244–252.
15 Z. Zhang, Z. Huang, X. Cheng, Q. Wang, Y. Chen, P. Dong, X. Zhang, *Appl. Surf. Sci.,* 2015, **355**, 45–51.
16 X. Li, Z. Zhuang, W. Li, H. Pan, *Appl. Catal. A Gen.,* 2012, **429–430**, 31–38.
17 C. Di Valentin, G. Pacchioni, A. Selloni, S. Livraghi, E. Giamello, *J. Phys. Chem. B.,* 2005, **109**, 11414–11419.
18 T. Phongamwong, M. Chareonpanich, J. Limtrakul, *Appl. Catal. B Environ.,* 2015, **168–169**, 114–124.
19 W.-J. Ong, L.-L. Tan, S.-P. Chai, S.-T. Yong, *Nano Res.,* 2014, **7**, 1528–1547.
20 C. Di Valentin, E. Finazzi, G. Pacchioni, A. Selloni, S. Livraghi, M. Cristina, E. Giamello, *Chem. Phys.,* 2007, **339**, 44–56.
21 A. J. Albrbar, A. Bjelajac, V. Djokić, J. Miladinović, D. Janaćković, R. Petrović, *J. Serbian Chem. Soc.,* 2014, **79**, 1127-1140
22 R. Petrović, N. Tanasković, V. Djokić, Ž. Radovanović, I. Janković-Častvan, I. Stamenković, D. Janaćković, *Powder Technol.,* 2012, **219**, 239–243.
23 A. J. Albrbar, V. Djokić, A. Bjelajac, J. Kovač, J. Ćirković, M. Mitrić, D. Janaćković, R. Petrović, *Ceram. Int*., 2016, **42**, 16718-16728.
24 S. Delavari, N. A. S. Amin, M. Ghaedi, J. Clean. Prod., 2016, **111**, 143–154.
25 J. Li, P. Yan, K. Li, J. You, H. Wang, W. Cui, W. Cen, Y. Chu, F. Dong, *J. Mater. Chem. A*, 2019, **7**, 17014-17021
26 P. Yan, J. Long, K. Li, S. Yuan, Y. Liu, Y. Chen, *Catal. Sci. Technol.*, 2019, **9**, 1451-1456
27 M. Sahu, P. Biswas, *Nanoscale Res. Lett.,* 2011, **6**, 1–14.
28 E.Y. Kim, D.S. Kim, B.T. Ahn, *Bull. Korean Chem. Soc.,* 2009, **30**, 193–198.
29 G. Kovács, L. Baia, A. Vulpoi, T. Radu, É. Karácsonyi, A. Dombi, K. Hernádi, V. Danciu, S. Simon, Z. Pap, *Appl. Catal. B Environ.,* 2014, **147**, 508–517.
30 T. Ohno, K. Sarukawa, K. Tokieda, M. Matsumura, *J. Catal.,* 2001, **203**, 82–86.
31 T. Ohno, K. Tokieda, S. Higashida, M. Matsumura, *Appl. Catal. A Gen.*, 2003, **244**, 383–391.
32 F. Amano, M. Nakata, A. Yamamoto, T. Tanaka, *Catal. Sci. Technol.,* 2016, **6**, 5693–5699
33 K. Kočí, L. Obalová, L. Matějová, D. Plachá, Z. Lacný, J. Jirkovský, O. Šolcová, *Appl. Catal. B Environ.,* 2009, **89** , 494–502.
34 K. Kočí, V. Matějka, P. Kovář, Z. Lacný, L. Obalová, *Catal. Today.,* 2011, **161**, 105–109.
35 H. Zhao, L. Liu, J.M. Andino, Y. Li, *J. Mater. Chem. A.,* 2013, **1**, 8209–8216.
36 L.-Y. Lin, S. Kavadiya, X. He, W.-N. Wang, B. Begum Karakocak, Y.-C. Lin, M. Y. Berezin, P. Biswas, *Chem. Eng. J.*, 2019, in press
37 J. Li, M. Zhang, Z. Guan, Q. Li, C. He, J. Yanga, *Appl. Catal. B Environ.*, 2017, **206**, 300–307
38 C. C. Lo, C. H. Hung, C. S. Yuan, J. F. Wu, Sol. *Energy Mater. Sol. Cells.,* 2007, **91**, 1765–1774.
39 M. Tasbihi, F. Fresno, U. Simon, I. J. Villar-García, V. Pérez-Dieste, C. Escudero, V. A. de la Peña O'Shea, *Appl. Catal. B: Environ.*, 2018, **239**, 68–76
40 L. Liu, Y. Li, *Aerosol Air Qual. Res.*, 2014, **14**, 453–469
41 V. P. Indrakanti, J. D. Kubicki, H. H. Schobert, *Energy Environ. Sci.,* 2009, **2**, 745–758.–582.
42 L. C. Grabow, A. A. Gokhale, S. T. Evans, J. A. Dumesic, M. Mavrikakis, *J. Phys. Chem. C.,* 2008, **112**, 4608–4617.
43 D. Kopač, M. Huš, M. Ogrizek, B. Likozar, *J. Phys. Chem. C.,* 2017, **121**, 17941–17949.
44 S. Delavari, N. A. S. Amin, *Appl. Energy,* 2016, **162**, 1171–1185.
45 M. Tahir, N. S. Amin, *Appl. Catal. A Gen.,* 2013, **467**, 483–496.